GEOPHYSICS

Rupture phases reveal geometry-related rupture propagation in a natural earthquake

Suli Yao[1] and Hongfeng Yang[1,2]*

Understanding and deciphering wiggles from seismograms has been a long endeavor to understand the internal structure of the Earth and to explore earthquake source properties. Here, we make an attempt to decipher the continuous rupture phases as large near-fault velocity pulses along the East Anatolian Fault in the 2023 moment magnitude (M_w) 7.8 Kahramanmaraş, Türkiye, earthquake. Through data analysis and dynamic rupture simulations, we robustly identify the transient supershear rupture on a segment with flat fault trace and rupture deceleration at fault bends. Our study highlights the complexity and superior application of near-fault data for understanding earthquake dynamics.

INTRODUCTION

Seismic waves are generated by activities with sudden movements inside or on the surface of the earth such as earthquakes, volcanos, and landslides. The waves propagate inside the earth and, therefore, carry the information of both the source and the Earth structure. Coherent wave phases on seismograms have been widely used to discover the Earth internal structure as demonstrated by numerous textbook examples such as the discovery of the Moho (*1*) and the solid inner core (*2*). In addition to structure imaging, seismic wave phases can provide direct information about the earthquake source, such as the location and the source mechanism.

Resolving detailed earthquake rupture processes from seismic waves is challenging, as the recorded data are the superposition of responses to continuous rupture processes, convolved with earth structure. Seismic wave–based approaches have been developed such as finite-fault slip inversion (FFI) (*3*, *4*) and back projection (BP) (*5*). FFI requires certain assumptions about the source (e.g., shape of slip rate function) and earth structure that potentially lead to intrinsic uncertainties (*6*, *7*). BP using teleseismic arrays or similar approaches based on near-field seismic networks (*8*) only requires waveform stacking to locate radiated energy. Nevertheless, the relation between the radiated energy and the rupture on the fault is ambiguous, and the results depend on array geometry and frequency content (*9*, *10*).

Stations in close proximity to faults are anticipated to record large velocity pulses during the passage of a rupture front. The pulses, termed the rupture phases, can reveal the slip and friction evolution on the fault without needing to implement an inversion procedure (*11*). Rupture phases are commonly viewed in dynamic rupture simulations (*12*, *13*) and laboratory experiments with sensor arrays on or near the frictional interfaces (*14*) or with ultrahigh-speed camera and digital imaging techniques (*15*). However, direct observations of rupture phases in natural earthquakes have been rare and mostly are only available on a single station (*16–18*), making it impossible to continuously track the rupture.

In addition, large earthquakes usually feature complex fault geometry, material properties, and rupture processes compared to laboratory experiments. For instance, irregular fault geometry, such as a bend, a bump, a branch, or a stepover, has been evidenced to control rupture initiation, propagation, and termination (*19–21*). Due to the lack of such continuous near-fault datasets in natural earthquakes, the impacts of those heterogeneities on near-fault rupture phases and whether those complex rupture behaviors can be resolved using near-fault rupture phases are unknown.

The near-fault strong motion records along the 120-km-long Amanos segment in the 2023 moment magnitude (M_w) 7.8 Kahramanmaras earthquake in Türkiye (Fig. 1) provide the first ever opportunity to investigate the coherent rupture phases in a natural earthquake. In this study, we aim to identify the rupture phases and demonstrate their application in rupture dynamics.

RESULTS

Large near-fault velocity pulses along the Amanos segment

On 6 February 2023, at 01:17 UTC, an M_w 7.8 left-lateral strike-slip earthquake initiated on a branch fault, with the hypocenter at (37.014°E, 37.226°N, 10 km deep), reported by United States Geological Survey. The rupture then transitioned into the East-Anatolian fault, the transform boundary between the Anatolian and Arabian plates (*22*, *23*), and propagated bilaterally with a final along-strike extent of ~300 km (Fig. 1) (*23*, *24*). Around 9 hours later, an M_w 7.5 earthquake occurred on another fault ~100 km northwest of the mainshock epicenter. These two events, together with several M6 aftershocks, caused tremendous damage to buildings and facilities in Türkiye and Syria and led to at least 52,800 deaths, making it one of the deadliest natural hazards.

The M_w 7.8 earthquake was well recorded by the local strong motion stations especially along the Amanos segment in the south with 10 stations located within 3 km to the surface trace (Fig. 1) [downloaded from Turkish Accelerometric Database and Analysis System of Disaster and Emergency Management Authority (AFAD-TADAS) website: https://tadas.afad.gov.tr]. We first inspect the data and correct the clock errors (see details in fig. S1). Then, we obtain the velocity waveforms by integrating the acceleration and rotate the waveforms to fault-parallel (FP) and fault-normal (FN) directions using the local strike for each station (fig. S2 to S4). The velocity waveforms are then filtered to below 1 Hz in the following analysis.

We observe large velocity pulses at these near-fault stations. As the near-field terms of ground motions decay markedly with distance

[1]Department of Earth and Environmental Sciences, The Chinese University of Hong Kong, Hong Kong, China. [2]Shenzhen Research Institute, The Chinese University of Hong Kong, Shenzhen, China.
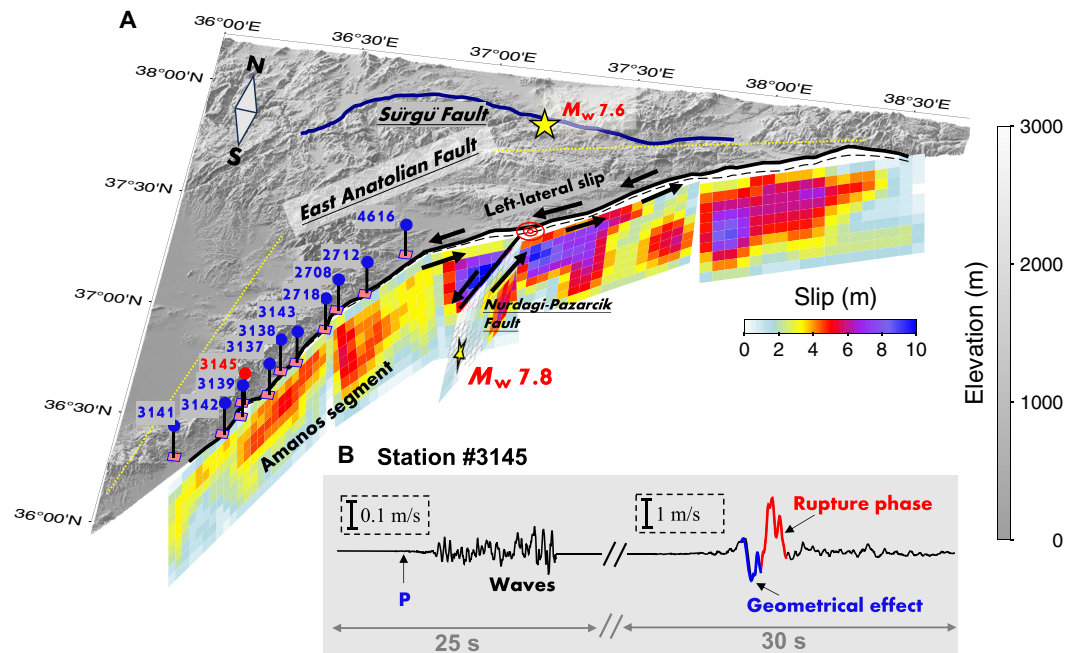*Corresponding author. Email: hyang@cuhk.edu.hk

Fig. 1. The near-fault observations for the 2023 Kahramanmaraş, Türkiye, M_w 7.8 earthquake. (**A**) A three-dimensional (3D) map view. The yellow stars mark the hypocenters of the M_w 7.8 and M_w 7.6 events, respectively. The pink squares represent the near-fault strong motion stations with their names written in blue. The 3D slip model is constructed mainly based on InSAR data (*24*). (**B**) Fault-parallel (FP) velocity waveform at station #3145. The onset of waves and the subsequent large velocity pulses are plotted using different amplitude scales. The pulses associated with the geometrical effect and the rupture phase are plotted in blue and red, respectively.

[velocity decays as $\frac{1}{R^4}$, where R is the distance; (*25*)], these large velocity pulses are dominated by local rupture along the Amanos segment, while the contributions from the splay fault and the northern segment are negligible. As shown in the data, the amplitude of the velocity pulse is over 10 times higher than the waves radiated from the splay fault at station #3145 (Fig. 1B). In addition, the spectrograms show no dispersion, and, therefore, these large pulses cannot be surface waves (fig. S5).

Some of the strong motion data have been used in previous studies to constrain the rupture characteristics, such as joint kinematic inversions (*22*, *26–29*) and dynamic rupture simulations (*30*, *31*). Likely due to the different inversion algorithms, data processing, data selection, and model parameterization, these kinematic models differ in rupture speed along the Amanos segment. Some studies used the velocity peaks or energy envelopes to derive an average propagation speed of 2.8 to 3.2 km/s (*26*, *27*, *31*). However, they ignored the complexities in the near-field data and the embedded information. For instance, multiple FP and FN pulses exist at some stations (e.g., #3145 and #2708), posing the question of which pulses are associated with the rupture front. Moreover, some studies suggest that the rupture along the Amanos segment was modulated by the geometrical barriers (*32*) or asperities (*29*). Whether such rupture complexities can be tracked and verified by rupture phases is unclear.

Here, we endeavor to extract coherent near-fault rupture phases in a natural earthquake and apply them to better understand rupture dynamics. To do so, we isolate the contributions of the rupture front and the geometrical effect through data analysis and dynamic rupture simulations. Then, we demonstrate the superior application of the identified phases in tracking the rupture propagation.

Near-fault rupture phase at different FN distances

To distinguish rupture details in the data, we first conduct a dynamic rupture simulation on a three-dimensional (3D) vertical strike-slip planar fault to demonstrate the relationship between typical near-fault velocity pulses and a rupture. Details of the model setup can be found in Materials and Methods and Supplementary Materials (fig. S6).

We investigate the features of velocity pulses during a subshear rupture. For the region that is sufficiently close (i.e., 0.2 km) to the fault, both FP and FN velocities show a single large pulse (Fig. 2A and fig. S7B). The FP pulse is an analog to the shallow slip rate pulse on the fault while the FN pulse is dominated by the energy carried by S waves that accumulate in front of the rupture (fig. S7) (*33*). Therefore, the FN pulse arrives slightly ahead of the FP, but the motion in the FP component is more sensitive to the local fault slip. The data recorded at stations #2712 (Fig. 2C) and #3138 (fig. S3) show typical features of this single-pulse scenario. Then, we can pick the onset of the FP pulse as the rupture time.

In contrast to the single pulse, we observe double FP pulses at some stations, which are associated with their relatively large FN distances (>1 km). As shown in our simulation, with the FN distance increasing, another FP pulse emerges ahead of the major FP pulse while the FN pulse remains single and resides between the two FP pulses (Fig. 2B). In this case, the first FP pulse is more associated with the energy ahead of the rupture zone and the second one is more dominated by fault slip. Moreover, according to our simulation, the onset of the second pulse is nearly fixed across different FN distances (0 to 3 km) and is consistent with the onset of the pulse in the single-pulse scenario (fig. S8D). The data on stations #2718 and #3137 are the typical cases of such double-pulse scenario (Fig. 2, E
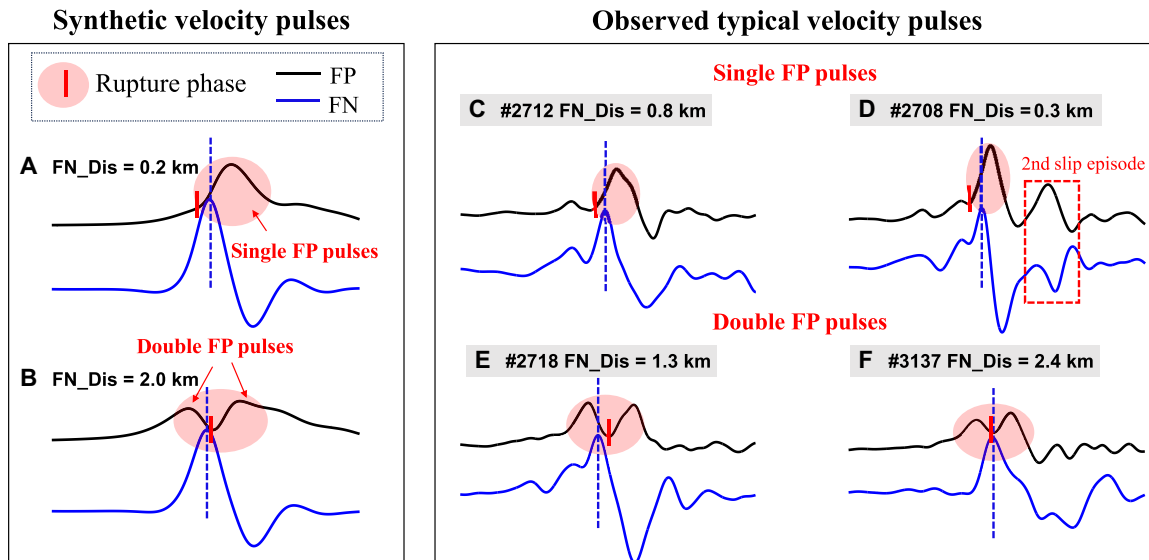
Fig. 2. Synthetic and observed typical near-fault velocity pulses. (**A**) The synthetic FP (black) and fault-normal (FN) (blue) velocity pulses at a very short FN distance (i.e., 0.2 km) in a subshear rupture. (**B**) The synthetic velocity pulses at a relatively long FN distance (i.e., 2.0 km). (**C** and **D**) The velocity pulses at stations #2712 and #2708 showing the typical single-FP-pulse feature. (**E** and **F**) The velocity pulses at stations #2718 and #3137 showing the typical double-FP-pulse feature. The short red bars mark the picked rupture time in the FP component. The vertical blue dashed lines mark the peaks of FN pulses. The red dashed box in (D) mark the pulses associated with a potential second slip episode near station #2708. All waveforms shown here are filtered to below 1 Hz.

and F). The single FN peak resides between the two FP peaks at the two stations (Fig. 2, E and F). We rule out other potential mechanisms such as slip heterogeneities, multiple rupture fronts, or geometrical effects for causing the double FP pulses at the two stations, because we do not observe any second FN pulses with similar durations and time shifts (3 to 5 s) as observed in the FP component (fig. S3). Furthermore, considering the size of the shallow low-velocity zone (up to 2 to 3 km), the effects of the fault zone structure are generally limited to frequency band of higher than 1 Hz in previous simulation results and observations (*12, 34, 35*). Therefore, the second FP pulses cannot be caused by fault zone structure. More detailed justifications can be found in the Supplementary Materials. To make a fair estimate for the rupture speed between stations with different FN distances, we thus pick the onset of the second FP pulse as the rupture time.

In addition, we observe atypical FP pulses at station #2708 (Fig. 2D), which is very close to the fault (i.e., 0.3 km) and, therefore, is anticipated to feature a single FP pulse. We infer that the first FP pulse is associated with the main rupture front as it follows the major FN pulse (fig. S2). The second FP pulse is accompanied by a smaller FN pulse with an opposite polarity. Considering their polarities, they are likely associated with a secondary left-lateral slip episode in the south to station #2708. The final extent of this episode should be between stations #2712 and #2718 as no similar FP pulses accompanied by FN pulses were observed (fig. S2). Therefore, we pin down the rupture time of the major rupture front at the onset of the first FP pulse at station #2708.

Rupture phase associated with fault bends

Except above stations with typical near-fault rupture phases, some stations (i.e., #4616 and #3145) feature atypical velocity pulses such as large negative FP velocity pulses and multiple FN velocity pulses

(fig. S2). After inspecting the final displacements and the particle motions, we prove that those negative pulses are not caused by potential mislocations of stations relative to the fault or polarity changes (fig. S3). It is unclear whether those complexities are associated with geometrical irregularities of fault bends or intrinsic rupture processes. In this section, we will investigate these pulses and their relationship with fault geometry and rupture propagation.

Here, we construct a multi-segment rupture model to investigate the impact of fault bends on near-fault velocity pulses. When the rupture encounters a bend, the original velocity pulse before encountering the bend keeps propagating along the previous trajectory, especially the FN pulse (see more details in the Supplementary Materials, fig. S9). Owing to the variations in strike, the original FN pulse may contribute a negative FP pulse after decomposition at the receiving stations, depending on the bending direction and the relative location of the station to the fault (Fig. 3A).

For instance, the changes of strike at the two bends before station #3145 are ~32° and ~22°, respectively (Fig. 3B), where multiple FP and FN velocity pulses are observed (Fig. 3, C and D). According to the decomposition results, we find that the negative FP pulse and the first FN pulse recorded at station #3145 are caused by segment #1. While the following positive FP and FN pulses are caused by segments #2 and #3. We then combine the pulses from all segments to recover the primary features of data. As shown in Fig. 3C, the negative FP pulse arrived 2 s earlier than the following positive FP pulse. The 2-s delay indicates that the rupture propagated from the first bending point to station #3145 at a speed substantially slower than the shear wave speed.

To further support the inference from the multi-segment model, we run dynamic rupture simulations for the rupture across the fault bend (Fig. 3E). Details of the dynamic models can be found in the Supplementary Materials. With the same initial stress condition, we
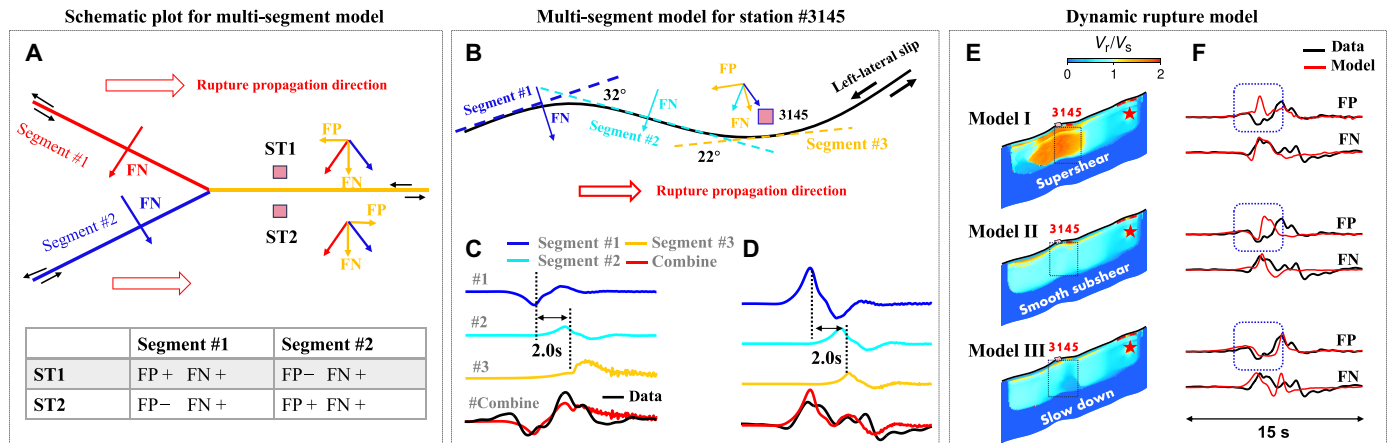
Fig. 3. The multi-segment model and dynamic rupture models for the rupture through bends near station #3145. (**A**) A schematic plot showing the rupture through bends in a left-lateral strike-slip fault system. The red and blue arrows indicate the orientations of the FN pulses generated by the two segments, respectively. The table concludes the polarities of FP and FN pulses received at stations ST1 and ST2 caused by segments #1 and #2. (**B**) The fault trace (black line) and the strikes of the three segments (dashed lines). The location of station #3145 is marked as a pink square. The orientations of the FN pulses from segments #1 and #2 are plotted as arrows in different colors, respectively. The orientations of the FN and FP at station #3145 are plotted as yellow arrows. (**C**) The contribution of the three segments and their combination (red) in FP velocity at station #3145. The observed FP velocity waveform is plotted in black. (**D**) Same with (C) but for the FN component. (**E**) The ratio of the rupture speed (V_r) to the shear wave velocity (V_s) in the three dynamic models. The location of station #3145 is marked as a pink square. The hypocenters are marked as red stars. (**F**) The comparison between the synthetic (red) and the observed (black) velocity waveforms at station #3145. The waveforms are normalized by the peak amplitudes and filtered to below 1 Hz.

modulate the frictional strength to obtain three dynamic models with different rupture speeds across the bend. When the rupture speed is supershear (model I in Fig. 3E), we observe a very narrow negative FP pulse ahead of the rupture phase and a single FN pulse (Fig. 3F). When the speed is subshear with no abrupt speed change (model II), the width of the negative FP pulse increases and double FN pulses emerge (Fig. 3F). In model III, the rupture decelerates at the bend with a rupture speed of ~2 km/s, leading to the best fit on the width of the FP pulse and the time delay between the two FN pulses (Fig. 3F). Similarly, we obtain the same conclusion of rupture deceleration at the fault bend near station #4616 (figs. S10 and S11). The dynamic rupture simulations, as well as the multi-segment models, highlight the application of the near-fault velocity field to illustrate rupture propagation in details.

Rupture propagation speeds inferred from rupture phases

By investigating the complex near-fault velocity field, we are able to identify the FP pulses associated with the rupture front as rupture phases on all near-fault stations along the Amanos segment (Fig. 4A). We then calculate the rupture speeds using the identified rupture time. Considering potential uncertainties introduced by different FN distances, we avoid estimates between neighboring stations. Instead, we divide the fault into three subsegments according to along-strike geometrical changes (Fig. 4B). The rupture propagates at a subshear speed (i.e., 3.1 km/s) between stations #4616 and #2718. After a geometrical bend, the rupture accelerates into supershear speed (4.3 km/s on average) between stations #2718 to #3137. Then, the rupture slowed down to subshear (i.e., 2.6 km/s) from stations #3137 to #3142 after encountering another fault bend.

The robustness of our determination of rupture velocity among station pairs has been further supported through dynamic rupture models (see more details in the Supplementary Materials, figs. S12 to S15). In the first model, we assume a depth-dependent stress and

friction condition on the fault without along-strike variations. In the second model, we prescribe a heterogeneous stress condition according to the coseismic stress drop distribution (see more details in the Supplementary Materials). The rupture propagation is relatively smooth with subshear speeds (~3.2 km/s) in both models. The apparent rupture phase propagating speed varies between 3.0 to 3.3 km/s between the three station pairs in the two models (figs. S12B and S14B). The speed changes identified in the data are 1.2 and 1.7 km/s (3.1 to 4.3 km/s; 4.3 to 2.6 km/s), much larger than the variations in the two reference models, suggesting that the observed marked speed changes are robust despite the geometrical effects and heterogeneous slip distribution.

DISCUSSION

Geometry-related transient supershear and rupture deceleration

Our study reveals the correlation between fault bends and rupture deceleration. The bend near station #4616 resides in the extensional regime (fig. S10) and, thus, is favored for rupture propagation due to the coseismic reduction of effective normal stress (36). The two bends near station #3145 are compressional and extensional, respectively (Fig. 3B). However, according to our results, the rupture slows down in both situations. Such observations suggest that the interaction between the dynamic stress field and fault bends does not solely depend on the bending direction. The shear stress perturbations across bends may also play a controlling role, which depends on the rupture speed (37). Moreover, fault structure such as the fault dip angle at the bends may also influence the dynamic stress field. In addition, the geometry-controlled pre-event stress and friction properties may be responsible, as kinematic models suggest reductions or discontinuities in fault slip across those bends (Fig. 1A). Our results provide constraints on the average rupture speed between the
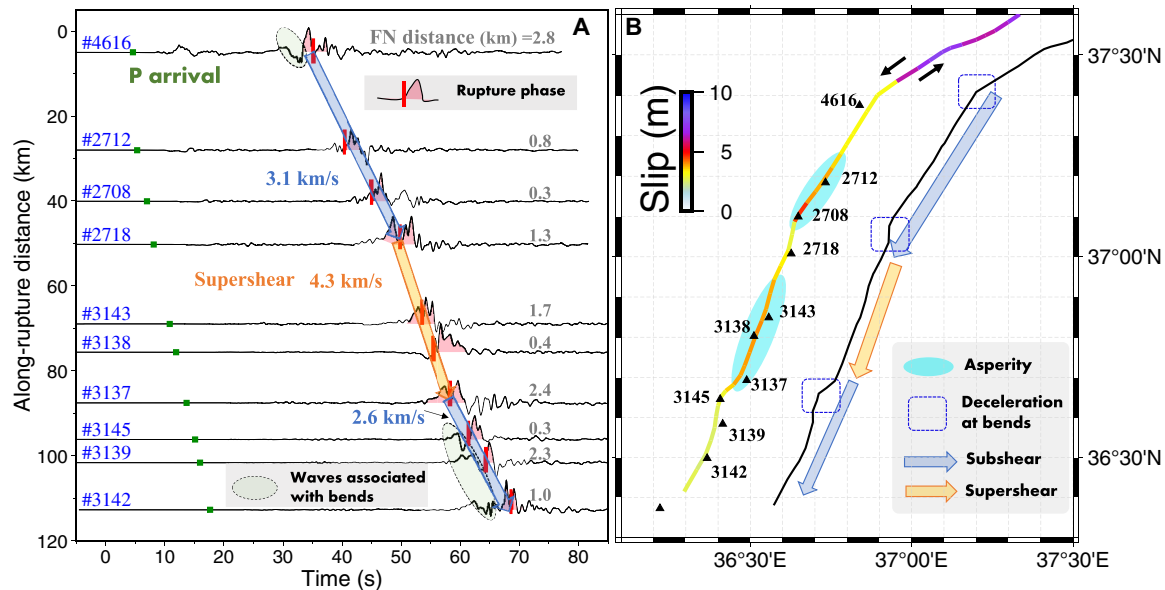
Fig. 4. Rupture phases and rupture propagation along the Amanos segment. (**A**) FP velocity waveforms. The FN distances for stations are written in gray in the right side. The green squares indicate the P arrivals on all stations. The rupture phases are shaded in pink. The short red bars mark the picked rupture time at the stations. The wiggles associated with fault bends are shaded by green ellipses. The arrows represent the rupture propagation with subshear (blue) and supershear (yellow) speeds and their average speeds. All waveforms shown here are filtered to below 1 Hz. (**B**) The rupture trace colored by the average slip in the top 5 km (*24*). The locations of the asperities are shaded in cyan. The bends are marked by blue dashed rectangles. The arrows represent the rupture propagation along the trace with subshear (blue) and supershear (yellow) rupture speeds.

bending points and the receiving stations. However, we note that the current station coverage cannot resolve detailed slip-stress evolution near the bends and responsible mechanisms for rupture deceleration. A dense network near the geometrical complexities of major faults is demanded to derive further detailed information.

The near-fault rupture phases provide a constraint on the geometry-related supershear transition. The supershear rupture speed emerges between stations #2718 and #3143 on a high-slip (high-stress-drop) asperity with a relatively flat fault trace, a favored condition for the rupture to speed up (*38–40*). Unlike long-sustaining supershear ruptures that can be robustly identified through BP (*41*), Mach pulse (*42*), or kinematic inversion (*43, 44*), such as in the 1979 M_w 6.5 Imperial Valley earthquake (*43*), the 1999 M_w 7.6 İzmit earthquake (*44*), and the 2001 M_w 7.8 Kokoxili earthquake (*45*), debates often exist for transient supershear propagation, in which no mature Mach cone was formed, such as the 2021 M_w 7.6 Maduo earthquake (*46, 47*) and the rupture along the Amanos segment in this M_w 7.8 event (*22, 26–32*). In this study, we do not observe long-duration supershear features of the velocity pulses at individual near-fault stations (fig. S3), which is reasonable for the nature of transient supershear propagation. Instead, we use the continuous network along the fault trace to track the rupture and identify a transient supershear speed. Compared to traditional approaches, our method avoids ambiguous inversion processes and provides additional constraints by extracting the most valuable information, the rupture phases.

Amplitudes of velocity pulses

The waveform comparisons in our study are all conducted after normalizing the amplitude, i.e., omitting the amplitude information but focusing on the phases. It has been suggested by laboratory experiments and theoretical models that the ratio between the amplitudes of near-fault FP and FN pulses might be an indicator for rupture speed (*33, 48*). However, its application on natural earthquakes remains controversial (*29, 49*). Through dynamic rupture simulations, we investigate the efficiency of the FP/FN ratio in identifying rupture speed transitions (see more info in the Supplementary Materials, figs. S16 to S19). Our modeling results suggest that the ratio cannot react simultaneously to rupture speed changes but needs a transition process, making it challenging to identify transient supershear propagation. Moreover, the ratio can be influenced by other factors such as the FN distance and the rupture front shape in addition to the geometrical effect discussed above. Therefore, we do not include the amplitude ratio as an indicator of rupture speed in this study.

In our results, we have identified an average supershear rupture speed (i.e., 4.3 km/s) between stations #2718 and #3137. However, the velocity pulses along this segment do not show any obvious supershear features (fig. S3), and their FP/FN ratios are all below 1. The possible scenario is that the supershear speed only existed at some portions of the segment. Because of the large station spacings of 8 to 18 km, especially between stations #2718 and #3143 (Fig. 4A), we are now not able to identify the exact locations of supershear transitions. Nevertheless, our data analyses and dynamic models highlight the robustness of near-fault rupture phases in tracking heterogeneous rupture propagation. On the basis of the rupture phases, we identify diverse rupture behaviors associated with fault geometry, including rupture deceleration and supershear transition. Our study can serve as guidance for future seismic network design and near-fault data analysis.

MATERIALS AND METHODS
Processing strong motion data
The strong motion data used in this study are downloaded from AFAD-TADAS website (https://tadas.afad.gov.tr). We check the P arrivals on all stations and compare them with the synthetic travel

time calculated from a regional 1D velocity model (table S1 and fig. S1B) (50). The differences between the picked P arrivals and synthetics are within 1 s except for stations #3142, #3137, #3138, #2718, and #4616 (fig. S1B). We suspect clock shifts and correct the clock by shifting the P arrivals to align with the synthetics. More details can be found in the Supplementary Materials.

The raw data are acceleration series. We first integrate the acceleration into velocity. The strong motion data bare baseline shifts under strong shaking, which is obvious when integrating the data into displacement. We inspect and correct the data following the method introduced by Wang et al. (51). The correction slightly influences the amplitude of the velocity pulses, while the timing and length of the velocity pulses are almost unaffected. We then rotate the velocity waveforms into the FP and FN directions (figs. S2 and S3) according to the local strike of fault trace (52). In this study, all analyses are based on the velocity waveforms.

Dynamic rupture simulations

We conduct a 3D dynamic rupture simulation on a vertical planar strike-slip fault embedded in a cubic elastic domain, which extends 180 km along strike, 80 km along the strike-normal direction, and 50 km in depth. The rupture extends along strike unilaterally for 100 km. The grid size on the fault is 150 m. A 1D velocity model (50) is adopted (table S1).

We adopt a slip-weakening friction law as the constitutive law on the fault (53). In this friction law, the frictional strength (τ_f) decreases linearly with fault slip (δ) and drops from yield stress (τ_s) to dynamic stress (τ_d) level when the slip reaches the critical weakening distance (D_0). We choose typical values of 0.7 and 0.4 for static (f_s) and dynamic friction (f_d) coefficients inside the seismogenic zone. The stress ratio inside the seismogenic zone ($S = \frac{\tau_s - \tau_i}{\tau_0 - \tau_d}$; $\tau_s = 35$ MPa, $\tau_i = 28$ MPa, $\tau_d = 20$ MPa) is 0.88. Outside the seismogenic zone, the fault is assumed to be strengthened during coseismic slip so the dynamic friction coefficient (i.e., 0.9) is set to be higher than the static coefficient. The seismogenic zone extends from 2 to 16 km in depth. We set the effective normal stress (σ_n) on the fault to be 50 MPa below 3 km and linearly decrease to zero at the free surface. We set the cohesion strength to be 3 MPa at the free surface and linearly decrease to 0 MPa in the top 3 km zone. D_0 is prescribed to be 1 m on the fault. All model parameters are plotted in fig. S6.

The nucleation zone is set to be at 9 km depth. We increase the initial shear stress to be 0.1 MPa higher than the yield stress inside a circular nucleation zone with a radius of 3 km. The rupture outside the nucleation zone is spontaneous under the control of the stress and friction evolution. We use a finite-element package, PyLith (version 2.2.2) (54), to run the simulation. The rupture first propagates with steady subshear velocity (fig. S7A). To stimulate a supershear transition, we increase the initial stress by 4 MPa between $x = 30$ and $x = 60$ at the depth of 6 to 16 km. The rupture then propagates with a steady supershear speed (fig. S7A).

In the dynamic rupture models across bends, we adopt same model inputs as in fig. S6 but different fault geometry (52). In addition, the nucleation is initiated by a time weakening mechanism with an initial rupture speed of 1.5 km/s. We modify the yield stress and D_0 near the bends to modulate the rupture speed across bends (see more details in the Supplementary Materials).

In the dynamic models for the whole Amanos segment, we adopt the curved fault trace constrained by InSAR (52). We first simulate with the same initial stress condition and frictional parameters shown in fig. S6. The dynamic rupture model turns to propagate with a fairly constant rupture speed of ~3.2 km/s (fig. S12A). Later, we prescribe the heterogeneous initial shear stress on the fault to recover the final slip distribution on the fault. In the heterogeneous model, we set the initial stress according to the slip distribution (Fig. 1A). We calculate the stress drop on the fault and assume the initial shear stress (τ_i) to be the summation of the stress drop ($\Delta\tau$) (fig. S13) and a uniform background dynamic stress ($\tau_d = 20$ MPa) (eq. S4). The D_0 is set to be 20% of the final slip (55, 56). The stress ratio (S) is set to be 0.8. We chose those parameters to match the average rupture speed on the Amanos segment (i.e., 3.2 km/s). More details can be found in the Supplementary Materials.

Supplementary Materials

This PDF file includes:
Supplementary Text
Table S1
Figs. S1 to S19

REFERENCES AND NOTES

1. A. Mohorovičić, Das Beben Vom 8. x. 1909. *Jahrb. Meteorol. Observ. Zagreb.* **9**, 1–63 (1910). [The earthquake of 8 October 1909].
2. I. Lehmann, P′. Publications du Bureau Central Séismologique International. A14 (3): 87–115 (1936).
3. S. Das, B. V. Kostrov, Inversion for seismic slip rate history and distribution with stabilizing constraints: Application to the 1986 Andreanof Islands earthquake. *J. Geophys. Res. Solid Earth* **95**, 6899–6913 (1990).
4. S. E. Minson, M. Simons, J. L. Beck, Bayesian inversion for finite fault earthquake source models I—Theory and algorithm. *Geophys. J. Int.* **194**, 1701–1726 (2013).
5. M. Ishii, P. M. Shearer, H. Houston, J. E. Vidale, Extent, duration and speed of the 2004 Sumatra-Andaman earthquake imaged by the Hi-net array. *Nature* **435**, 933–936 (2005).
6. S. Hartzell, P. Liu, C. Mendoza, C. Ji, K. M. Larson, Stability and uncertainty of finite-fault slip inversions: Application to the 2004 Parkfield, California, earthquake. *Bull. Seismol. Soc. Am.* **97**, 1911–1934 (2007).
7. H. N. Razafindrakoto, P. M. Mai, Uncertainty in earthquake source imaging due to variations in source time function and earth structure. *Bull. Seismol. Soc. Am.* **104**, 855–874 (2014).
8. P. Spudich, E. Cranswick, Direct observation of rupture propagation during the 1979 Imperial Valley earthquake using a short baseline accelerometer array. *Bull. Seismol. Soc. Am.* **74**, 2083–2114 (1984).
9. L. Meng, J.-P. Ampuero, Y. Luo, W. Wu, S. Ni, Mitigating artifacts in back-projection source imaging with implications for frequency-dependent properties of the Tohoku-Oki earthquake. *Earth Planets Space* **64**, 1101–1109 (2012).
10. B. Li, B. Wu, H. Bao, D. D. Oglesby, A. Ghosh, A.-A. Gabriel, L. Meng, R. Chu, Rupture heterogeneity and directivity effects in back-projection analysis. *J. Geophys. Res. Solid Earth* **127**, e2021JB022663 (2022).
11. E. Fukuyama, T. Mikumo, Slip-weakening distance estimated at near-fault stations. *Geophys. Res. Lett.* **34**, 2–6 (2007).
12. X. Chen, H. Yang, Effects of seismogenic width and low-velocity zones on estimating slip-weakening distance from near-fault ground deformation. *Geophys. J. Int.* **223**, 1497–1510 (2020).
13. E. M. Dunham, R. J. Archuleta, Evidence for a supershear transient during the 2002 Denali fault earthquake. *Bull. Seismol. Soc. Am.* **94**, S256–S268 (2004).
14. S. Xu, E. Fukuyama, F. Yamashita, H. Kawakata, K. Mizoguchi, S. Takizawa, Fault strength and rupture process controlled by fault surface topography. *Nat. Geosci.* **16**, 94–100 (2023).
15. V. Rubino, A. J. Rosakis, N. Lapusta, Spatiotemporal properties of sub-Rayleigh and supershear ruptures inferred from full-field dynamic imaging of laboratory experiments. *J. Geophys. Res. Solid Earth* **125**, e2019JB018922 (2020).
16. Y. Kaneko, E. Fukuyama, I. J. Hamling, Slip-weakening distance and energy budget inferred from near-fault ground deformation during the 2016 Mw7.8 Kaikōura earthquake. *Geophys. Res. Lett.* **44**, 4765–4773 (2017).
17. E. Fukuyama, W. Suzuki, Near-fault deformation and Dc″ during the 2016 Mw7.1 Kumamoto earthquake. *Earth Planets Space* **68**, 194 (2016).

18. X. Chen, H. Yang, M. Jin, Inferring critical slip-weakening distance from near-fault accelerogram of the 2014 Mw 6.2 Ludian earthquake. *Seismol. Res. Lett.* **92**, 3416–3427 (2021).

19. G. King, J. Nábělek, Role of fault bends in the initiation and termination of earthquake rupture. *Science* **228**, 984–987 (1985).

20. A. J. Elliott, M. E. Oskin, J. Liu-Zeng, Y. Shao, Rupture termination at restraining bends: The last great earthquake on the Altyn Tagh Fault. *Geophys. Res. Lett.* **42**, 2164–2170 (2015).

21. H. Yang, Y. Liu, J. Lin, Effects of subducted seamounts on megathrust earthquake nucleation and rupture propagation. *Geophys. Res. Lett.* **39**, L24302 (2012).

22. D. Melgar, T. Taymaz, A. Ganas, B. Crowell, T. Öcalan, M. Kahraman, V. Tsironi, S. Yolsal-Çevikbilen, S. Valkaniotis, T. S. Irmak, T. Eken, C. Erman, B. Özkan, A. H. Dogan, C. Altuntaş, Sub- and super-shear ruptures during the 2023 Mw 7.8 and Mw 7.6 earthquake doublet in SE Türkiye. *Seismica* **2**, 10.26443/seismica.v2i3.387 (2023).

23. N. G. Reitman, R. W. Briggs, W. D. Barnhart, J. A. Thompson Jobe, C. B. DuRoss, A. E. Hatem, R. D. Gold, S. Akçiz, R. D. Koehler, J. D. Mejstrik, C. Collett, Fault rupture mapping of the 6 February 2023 Kahramanmaraş, Türkiye, earthquake sequence from satellite data (ver. 1.1, February 2024) (U.S. Geological Survey data release, 2024); https://doi.org/10.5066/P985I7U2.

24. Z. Ma, C. Li, Y. Jiang, Y. Chen, X. Yin, Y. Aoki, S.-H. Yun, S. Wei, Space geodetic insights to the dramatic stress rotation induced by the February 2023 Turkey-Syria earthquake doublet. *Geophys. Res. Lett.* **51**, e2023GL107788 (2024).

25. K. Aki, P. G. Richards, *Quantitative Seismology* (University Science Books, 2002).

26. Z. Jia, Z. Jin, M. Marchandon, T. Ulrich, A.-A. Gabriel, W. Fan, P. Shearer, X. Zou, J. Rekoske, F. Bulut, A. Garagon, Y. Fialko, The complex dynamics of the 2023 Kahramanmaraş, Turkey, Mw 7.8-7.7 earthquake doublet. *Science* **381**, 985–990 (2023).

27. L. Xu, S. Mohanna, L. Meng, C. Ji, J.-P. Ampuero, Z. Yunjun, M. Hasnain, R. Chu, C. Liang, The overall-subshear and multi-segment rupture of the 2023 Mw7. 8 Kahramanmaraş, Turkey earthquake in millennia supercycle. *Commun. Earth Environ.* **4**, 379 (2023).

28. C. Liu, T. Lay, R. Wang, T. Taymaz, Z. Xie, X. Xiong, T. S. Irmak, M. Kahraman, C. Erman, Complex multi-fault rupture and triggering during the 2023 earthquake doublet in southeastern Türkiye. *Nat. Commun.* **14**, 5564 (2023).

29. B. Delouis, M. van den Ende, J. P. Ampuero, Kinematic Rupture Model of the 6 February 2023 Mw 7.8 Türkiye earthquake from a large set of near-source strong-motion records combined with GNSS offsets reveals intermittent supershear rupture. *Bull. Seismol. Soc. Am.* **114**, 726–740 (2024).

30. Z. Wang, W. Zhang, T. Taymaz, Z. He, T. Xu, Z. Zhang, Dynamic rupture process of the 2023 Mw 7.8 Kahramanmaraş earthquake (SE Türkiye): Variable rupture speed and implications for seismic hazard. *Geophys. Res. Lett.* **50**, e2023GL104787 (2023).

31. C. Ren, Z. Wang, T. Taymaz, N. Hu, H. Luo, Z. Zhao, H. Yue, X. Song, Z. Shen, H. Xu, J. Geng, W. Zhang, T. Wang, Z. Ge, T. S. Irmak, C. Erman, Y. Zhou, Z. Li, H. Xu, B. Cao, H. Ding, Supershear triggering and cascading fault ruptures of the 2023 Kahramanmaraş, Türkiye, earthquake doublet. *Science* **383**, 305–311 (2024).

32. Y. Zhang, X. Tang, D. Liu, T. Taymaz, T. Eken, R. Guo, Y. Zheng, J. Wang, H. Sun, Geometric controls on cascading rupture of the 2023 Kahramanmaraş earthquake doublet. *Nat. Geosci.* **16**, 1054–1060 (2023).

33. E. M. Dunham, R. J. Archuleta, Near-source ground motion from steady state dynamic rupture pulses. *Geophys. Res. Lett.* **32**, (2005).

34. V. F. Cormier, P. Spudich, Amplification of ground motion and waveform complexity in fault zones: Examples from the San Andreas and Calaveras faults. *Geophys. J. Int.* **79**, 135–152 (1984).

35. J. Song, H. Yang, Seismic site response inferred from records at a dense linear array across the Chenghai fault zone, Binchuan, Yunnan. *J. Geophys. Res. Solid Earth* **127**, e2021JB022710 (2022).

36. J. C. Lozos, D. D. Oglesby, B. Duan, S. G. Wesnousky, The effects of double fault bends on rupture propagation: A geometrical parameter study. *Bull. Seismol. Soc. Am.* **101**, 385–398 (2011).

37. A. N. B. Poliakov, R. Dmowska, J. R. Rice, Dynamic shear rupture interactions with fault bends and off-axis secondary faulting. *J. Geophys. Res. Solid Earth* **107**, ESE 6-1–ESE 6-18 (2002).

38. E. M. Dunham, Conditions governing the occurrence of supershear ruptures under slip-weakening friction. *J. Geophys. Res. Solid Earth* **112**, B07302 (2007).

39. Y. Kaneko, N. Lapusta, Supershear transition due to a free surface in 3-D simulations of spontaneous dynamic rupture on vertical strike-slip faults. *Tectonophysics* **493**, 272–284 (2010).

40. M. Bouchon, H. Karabulut, M.-P. Bouin, J. Schmittbuhl, M. Vallée, R. Archuleta, S. Das, F. Renard, D. Marsan, Faulting characteristics of supershear earthquakes. *Tectonophysics* **493**, 244–253 (2010).

41. H. Bao, L. Xu, L. Meng, J. P. Ampuero, L. Gao, H. Zhang, Global frequency of oceanic and continental supershear earthquakes. *Nat. Geosci.* **15**, 942–949 (2022).

42. H. Bao, J.-P. Ampuero, L. Meng, E. J. Fielding, C. Liang, C. W. D. Milliner, T. Feng, H. Huang, Early and persistent supershear rupture of the 2018 magnitude 7.5 Palu earthquake. *Nat. Geosci.* **12**, 200–205 (2019).

43. R. J. Archuleta, A faulting model for the 1979 Imperial Valley earthquake. *J. Geophys. Res. Solid Earth* **89**, 4559–4585 (1984).

44. M. Bouchon, N. Toksöz, H. Karabulut, M.-P. Bouin, M. Dietrich, M. Aktar, M. Edie, Seismic imaging of the 1999 Izmit (Türkiye) rupture inferred from the near-fault recordings. *Geophys. Res. Lett.* **27**, 3013–3016 (2000).

45. Y.-Y. Wen, K.-F. Ma, T.-R. A. Song, W. D. Mooney, Validation of the rupture properties of the 2001 Kunlun, China (M_s = 8.1), earthquake from seismological and geological observations. *Geophys. J. Int.* **177**, 555–570 (2009).

46. H. Yue, Z.-K. Shen, Z. Zhao, T. Wang, B. Cao, Z. Li, X. Bao, L. Zhao, X. Song, Z. Ge, C. Ren, W. Lu, Y. Zhang, J. Liu-Zeng, M. Wang, Q. Huang, S. Zhou, L. Xue, Rupture process of the 2021 M7.4 Maduo earthquake and implication for deformation mode of the Songpan-Ganzi terrane in Tibetan Plateau. *Proc. Natl. Acad. Sci. U.S.A.* **119**, e2116445119 (2022).

47. S. Wei, H. Zeng, Q. Shi, J. Liu, H. Luo, W. Hu, Y. Li, W. Wang, Z. Ma, J. Liu-Zeng, T. Wang, Simultaneous rupture propagation through fault bifurcation of the 2021 Mw7.4 Maduo earthquake. *Geophys. Res. Lett.* **49**, e2022GL100283 (2022).

48. M. Mello, H. S. Bhat, A. J. Rosakis, Spatiotemporal properties of Sub-Rayleigh and supershear rupture velocity fields: Theory and experiments. *J. Mech. Phys. Solids* **93**, 153–181 (2016).

49. M. Abdelmeguid, C. Zhao, E. Yalcinkaya, G. Gazetas, A. Elbanna, A. Rosakis, Dynamics of episodic supershear in the 2023 M7.8 Kahramanmaraş/Pazarcik earthquake, revealed by near-field records and computational modeling. *Commun. Earth Environ.* **4**, 456 (2023).

50. S. E. Güvercin, H. Karabulut, A. Ö. Konca, U. Doğan, S. Ergintav, Active seismotectonics of the East Anatolian fault. *Geophys. J. Int.* **230**, 50–69 (2022).

51. R. Wang, B. Schurr, C. Milkereit, Z. Shao, M. Jin, An improved automatic scheme for empirical baseline correction of digital strong-motion records. *Bull. Seismol. Soc. Am.* **101**, 2029–2044 (2011).

52. L. He, G. Feng, W. Xu, Y. Wang, Z. Xiong, H. Gao, X. Liu, Coseismic kinematics of the 2023 Kahramanmaras, Turkey earthquake sequence from InSAR and optical data. *Geophys. Res. Lett.* **50**, e2023GL104693 (2023).

53. Y. Ida, Cohesive force across the tip of a longitudinal-shear crack and Griffith's specific surface energy. *J. Geophys. Res.* **77**, 3796–3805 (1972).

54. B. T. Aagaard, M. G. Knepley, C. A. Williams, A domain decomposition approach to implementing fault slip in finite-element models of quasi-static and dynamic crustal deformation. *J. Geophys. Res. Solid Earth* **118**, 3059–3079 (2013).

55. J. R. Rice, Heating and weakening of faults during earthquake slip. *J. Geophys. Res. Solid Earth* **111**, B05311 (2006).

56. R. C. Viesca, D. I. Garagash, Ubiquitous weakening of faults due to thermal pressurization. *Nat. Geosci.* **8**, 875–879 (2015).